International Journal on Recent and Innovation Trends in Computing and Communication
ISSN: 2321-8169 Volume: 11 Issue: 9
***Article Received:** 25 July 2023 **Revised:** 12 September 2023 **Accepted:** 30 September 2023*

Thermal Image-Based Hotspot Detection System in Solar Panels by Lilnet-5 and Relu6-F-Rcnn

P.Pradeep Kumar[1] , Dr.M.Rama Prasad Reddy[2]
[1]Research Scholar
G.Pullaiah College of Engineering and Technology
Kurnool,Andhra Pradesh, India.
Mail Id: poluripradeep238@gmail.com
[2]Professor,EEE Dept.,
G.Pullaiah College of Engineering & Technology
Kurnool, Andhra Pradesh, India
Mail Id : mrpreddy77@gmail.com

Abstract: The effects of high temperatures are the hotspots that occur in solar panels. In previous works, the particular hotspot-affected panel detection on a large scale and the damage-percentage analysis are not concentrated. Hence, this article proposes an efficient detection system for solar panel hotspot identification from thermal images. To convert Photovoltaic (PV) power from one voltage to another voltage level, solar PV panels are employed and connected with the DC-DC converter. The Student T Distributed-Osprey Optimization Algorithm (ST-OOA) is utilized for controlling the converter duty cycle. The output obtained from the converter is in a signal waveform that is converted into a snowflake image by a Symmetrized Dot Pattern (SDP) and given to the LeCun Initialized LeNet-5 (LILNet-5) classifier for fault-panels detection. Afterward, the fault panels' thermal images are preprocessed along with faults and cracks segmentation by utilizing Rectified Linear Unit 6 Activated Faster Region-based Convolutional Neural Network (ReLu6-F-RCNN). Lastly, to identify the damage percentage of solar panels, power loss is calculated. Moreover, the performance analysis exhibited the framework's robustness in effective solar panel hotspot detection.

Keywords: Rectified Linear Unit 6 Activated Faster *Region-based Convolutional Neural Network* (ReLu6-F-RCNN), LeCun Initialized LeNet-5 Classifier (LILNet-5), Student T Distributed- Osprey Optimization Algorithm (ST-OOA), Symmetrized Dot Pattern (SDP), Maximum Power Point Tracker (MPPT).

1. INTRODUCTION

The sunlight energy will be converted into electrical energy by the PV module; also, they are implemented on a large scale nowadays, thus the maintenance will be complex (Afifah et al., 2021) (Pathak et al., 2022). Owing to the atmospheric conditions, hotspots are generated in the solar panels (Phoolwani et al., 2020). Such hotspots are identified by imaging techniques and analyzing temperature distribution patterns (Kandeal et al., 2021).

To detect hotspots in the PV module, temperature distribution and Thermographic Image (TI) based fault identification in PV modules are effective approaches (Rahaman et al., 2020) (Afifah et al., 2020). TI represents the image grounded on the PV module surface temperature distribution (Vergura, 2021)(Chen et al., 2020). The process involves the automatic detection of hotspots utilizing image processing approaches, incorporating neural networks and machine learning techniques (Venkatesh et al., 2022). Masking the affected areas in the PV module is the next step after detecting the hotspots. Lastly, for effective fault location identification and rectification, fault segmentation is achieved (Pramana & Dalimi, 2020). Nevertheless, the previous work only considered the micro-cracks and did not concentrate on other types of cracks. To address this issue, a novel ReLu6-F-RCNN framework for the solar panel hotspot detection system is proposed.

1.1 Problem Statement

The drawbacks of the prevailing works are described further:

- In previous works, damage level analysis and fault detection on a large scale are challenging.
- In existing work, only the micro crack-affected PV module was detected, but other cracks are less focused.
- Hotspots along with internal circuitry discoloration are the causes of energy loss in PV modules.

The proposed system's major objectives are,

Article Received: 25 July 2023 **Revised:** 12 September 2023 **Accepted:** 30 September 2023

- To efficiently classify the hotspot by utilizing the LILNet-5 classifier and its damage percentage estimation.
- To accurately segment the multiple cracks on the PV system, the ReLu6-F-RCNN approach is employed.
- The Maximum Power Point Tracker (MPPT) control system is connected to avoid the internal circuitry discoloration issue.

The structure of this paper is given as: Section 2 delves into the associated works; the proposed system is delineated in Section 3; Section 4 showcases the results; lastly, the paper is wrapped up in Section 5.

2. LITERATURE SURVEY

(Su et al., 2021) deployed a Residual Channel-wise Attention Gate Network (RCAG-Net) for the PV farms' hotspot detection system. To reduce the feature dimension, the model utilized global average pooling and multilayer perception operation. Hence, the RCAG-Net had a high potential in detecting the hotspot defects. This model could not ensure the exact pinpointing of all defects within PV modules owing to the inevitability of positioning errors.

(Zefri et al., 2022) established the three-layer deep learning system to classify defects in PV modules. VGG-16 architecture was employed by this model to classify the temperature pattern. Afterward, infrared thermal images were chosen from various PV sites and subjected to preprocessing utilizing the Structure from Motion – MultiView Stereo photogrammetric process. Even though the model attained a high F1-Score, it failed to detect the temperature variability in the PV module, thus affecting the overall performance of the system.

(Wang et al., 2022) explored a PV panel condition monitoring grounded on infrared detection. For image segmentation and effective fault classification, this approach employed the U-Net architecture and decision tree algorithm. Therefore, the model attained high fault detection accuracy. However, the model complexity was increased by utilizing the decision tree algorithm.

(Espinosa et al., 2020) elucidated an automatic physical fault classification of PV panels by utilizing a Convolutional Neural Network (CNN). The presented approach extracted, segmented, and classified the panel object from the RGB PV panel images utilizing CNN. Hence, the faulty PV panels were effectively classified by the suggested model. Yet, the model attained low accuracy since the collected dataset was very small.

(Hong et al., 2022) proffered PV plant defect detection system centered on visible and infrared images. For image segmentation purposes, the model employed the You Only Look Once version 5 (YOLOv5). The performance of this model attained high detection efficiency. Nevertheless, the intense reflectivity of the PV module caused a misclassification problem.

3. PROPOSED METHODOLOGY FOR DETECTING SOLAR PANEL HOTSPOTS

In this framework, an efficient solar panel hotspot detection system by LILNet-5 and ReLu6-F-RCNN is established. The proposed structure is displayed in Figure 1.

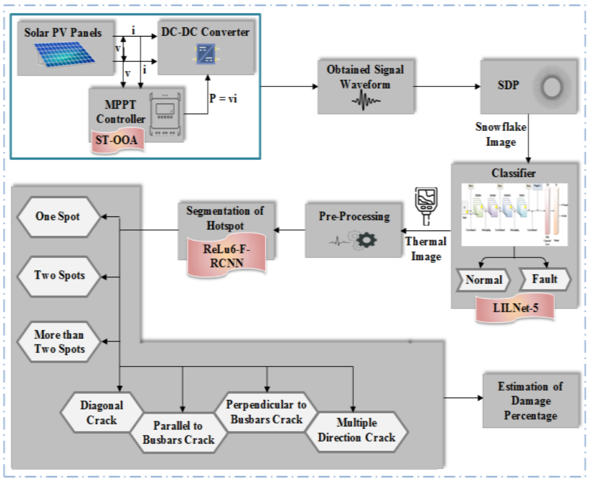

Figure 1: Proposed system structure

3.1. DC-DC converter

Large solar panels, which convert solar energy into electricity by PV cells, are established by the proposed system. After that, the DC-DC converter is connected for constant output voltage regulation. Then, the MPPT controller controls the converter's duty cycle. MPPT controller collects solar panel voltage and loads the converter with its optimum power requirements that are estimated by ST-OOA for their better exploration and exploitation. However, random position updation of the Osprey Optimization Algorithm (OOA) results in non-continuous semi-optimal solutions. Therefore, the Student T Distribution function is employed for its ability to estimate the population within a smaller sample size.

Initialization

The population of the osprey (O) is the power (product of voltage and current), and the osprey's position is the optimal power in the search space, which is expressed as,

$$O = \begin{Bmatrix} O_{11} & O_{12} \cdots & O_{1n} \\ O_{21} & O_{22} \cdots & O_{2n} \\ \vdots & \vdots & \vdots \\ O_{m1} & O_{m2} \cdots & O_{mn} \end{Bmatrix}, \; i = (1,2,\ldots\ldots, m), \; j = (1,2,\ldots\ldots, n) \quad (1)$$

$$O_{ij} = L_j + \circ_{ij} \times \left(U_j - L_j\right) \quad (2)$$

Here, O_{ij} signifies the i^{th} osprey in m number of osprey in the j^{th} search place of n dimensional search place; $U \; and \; L$ are the search place's upper and lower bounds. Maximum power (ℓ) is the fitness $(\Im)$ of osprey, which is represented as,

$$\Im = \max\{\ell\} \tag{3}$$

Location identification (exploration)

The set of fishes (F) that are the prey to be hunted by the O_{ij} is described as,

$$FO_i = \{F_k(O_k) < F_i\} \cup (O_{best}), \quad k \in \{1,2,....., m\} \tag{4}$$

Here, O_k symbolizes the random new k^{th} osprey; FO_i is the fish for the i^{th} osprey; F_k and F_i are the fish for k^{th} and i^{th} osprey; O_{best} is the best osprey. From (F), the osprey selected a fish and hunted it. During the hunting process, the position is updated as,

$$O_{ij}^{ex1} = O_{ij} + {}^{\circ}{}_{ij} \times \left(F_{s,ij} - rand * O_{ij}\right) \tag{5}$$

$$O_i^* = \begin{cases} O_i^{ex1}, & if \;\; \Im < F_i \\ O_i^*, & else \end{cases} \tag{6}$$

Here, O_{ij}^{ex1} is the position of the i^{th} osprey in the j^{th} search place based on the exploration phase; $F_{s,ij}$ implies the selected fish; $rand$ is the random numbers from the set $\{1,2\}$; O_i^* signifies the new position of the i^{th} osprey.

Relocate the fish (exploitation)

After hunting the prey, the osprey carried it to another location to eat it, which is estimated through the Student T Distribution function as,

$$O_{ij}^{ex2} = O_{ij} + \frac{L_j + {}^{\circ}{}_1\left(U_j - L_j\right) \cdot \sigma}{\sqrt{z}\left(\bar{q} - \mu\right)} \tag{7}$$

Here, O_{ij}^{ex2} is the osprey's position in exploitation; ${}^{\circ}{}_1$ is a random number; σ epitomizes sample standard deviation; z is the sample size; $\bar{q}$ is the sample mean, and μ is the population mean. The repetition of the above phases continues until the optimal power is obtained. After obtaining the optimal power, it is given to the DC-DC converter. Afterward, the converter generates regulated output voltage characteristics as a signal waveform.

3.2. SDP

The SDP transforms the generated waveform into a snowflake image (ψ). The signal (Q) with W sample-point created from DC-DC is represented as,

$$Q_W = \{Q_1, Q_2, ..., Q_w\} \tag{8}$$

Where, w exemplifies the total number of sample points; W in Q is mapped to polar-coordinates point $(\Re)$, which is expressed as,

$$\Re \to \Re\left[p_r(W), \theta(W), \varphi(W)\right] \tag{9}$$

Here, $p_r(W)$ is the polar radius of ψ; $\theta(W) \; and \; \varphi(W)$ are the two rotation angles of conventional polar space. The sample-point mapping is combined with the plotting gain $(\aleph)$, and the $\aleph$ condition is given as,

$$\aleph \le \theta \tag{10}$$

$$p_r(W) = \frac{Q_W - Q_{\min}}{Q_{\max} - Q_{\min}} \tag{11}$$

$$\theta(W) = \theta_\partial + \left(\frac{Q_{W+\tau} - Q_{\min}}{Q_{\max} - Q_{\min}}\right)\aleph \tag{12}$$

$$\varphi(W) = \theta_\partial - \left(\frac{Q_{W+\tau} - Q_{\min}}{Q_{\max} - Q_{\min}}\right)\aleph \tag{13}$$

Here, $Q_{\min} \; and \; Q_{\max}$ are the minimum and maximum of Q, τ epitomizes time-lag coefficient, and θ_∂ signifies the ∂^{th} rotational angle of the Z number of mirror symmetric planes, and it is exemplified as,

$$\theta_\partial = \frac{360}{Z} \tag{14}$$

From the above analysis, ψ is derived from Q in Z mirror planes of $\Re$ according to θ_∂.

3.3. Classifier

Thereafter, for classifying the normal and fault panels, ψ is given as input to the LILNet-5 classifier. The LeNet-5 was utilized for its lightweight design with a less complex structure. However, LeNet-5 has an unbalanced weight initialization issue that caused a vanishing gradient problem. Thus, LeCun weight initialization is employed, which prevents the gradient problems by setting constant variance.

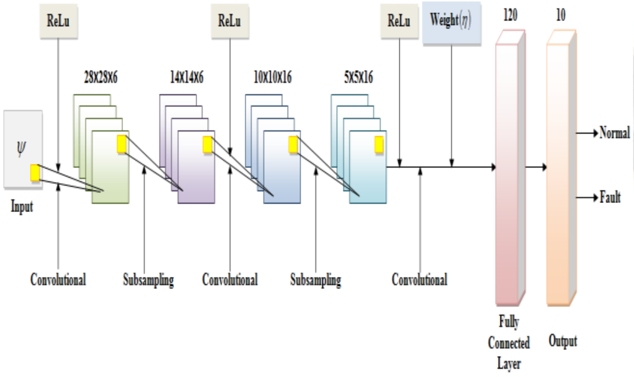

Figure 2: LILNet-5 architecture

3.3.1. Convolutional layer

The convolutional layers $(\wp)$ perform the feature extraction process; also, each layer comprises several convolutional kernels $(\Diamond)$. The input ψ gets connected with $\Diamond$ of this layer, which is represented as,

$$\psi = \{\psi_{a,b},\ \forall\ a = 1,2,..., A;\ b = 1,2,..., B\} \tag{15}$$

Here, A, B are the numbers of features in a, b from ψ, correspondingly; $\Diamond$ can be signified with the total size (E) as given below:

$$\Diamond = \begin{pmatrix} \Diamond_{1,1} & \Diamond_{1,2} \cdots \Diamond_{1,N} \\ \Diamond_{2,1} & \Diamond_{2,2} \cdots \Diamond_{2,N} \\ \vdots & \vdots \quad\quad \vdots \\ \Diamond_{M,1} & \Diamond_{M,2} \cdots \Diamond_{M,N} \end{pmatrix} \quad \forall\ M = 1,2,....., E-1;\ N = 1,2,....., E-1 \tag{16}$$

Here, M, N symbolize the layer's height and width; the $\wp$ operation is given as,

$$\wp = \Theta\left(\sum\nolimits_{M,N\in\Diamond} \Diamond_{M,N} \cdot \psi_{A+M,B+N} + \varepsilon_1\right) \tag{17}$$

Wherein, ε_1 symbolizes the offset, and Θ epitomizes the ReLu activation function used for its non-linearity properties, which is denoted as,

$$\Theta(\psi) = \max(0, \psi) \tag{18}$$

3.3.2. Sub-sampling layer

The sub-sampling layer $(\hbar)$ selects the features by down-sampling (ϑ_{down}) the dimensions of $\wp$ outputs that retain the maximum $(\max)$ values in the pooled area (G) as,

$$\hbar = \vartheta_{down}\{\max(g_{p,q})\} \tag{19}$$

Here, g symbolizes elements of G with the parameters $p, q \in G$.

3.3.3. Fully connected layer

The fully connected layer $(ƛ)$ can integrate the local information for discriminating the output classes. The $ƛ$ with Δ elements and ε_2 offset is expressed as,

$$ƛ = \eta \times \Delta + \varepsilon_2 \tag{20}$$

Where, η epitomizes LeCun weight initialization with weights (ν). It is defined as,

$$\eta = \sqrt{\frac{1}{\nu}} \tag{21}$$

3.3.4. Output layer

The output layer (Ω) mapped $ƛ$ to the probability within $(0,1)$ is elucidated as,

$$\Omega = \Xi(\eta \times \zeta + \varepsilon_3) \tag{22}$$

Here, ζ symbolizes Ω elements, ε_3 implies offset term, and Ξ specifies a softmax function for different classification classes as,

$$\Xi = \{\Xi_e^f \mid \forall e = 1,2,..., K,\ f = 1,2,...., L\} \tag{23}$$

International Journal on Recent and Innovation Trends in Computing and Communication
ISSN: 2321-8169 Volume: 11 Issue: 9
***Article Received:** 25 July 2023 **Revised:** 12 September 2023 **Accepted:** 30 September 2023*

Where, Ξ_e^f notates the probability of f^{th} sample for the e number of classification classes, and K, L signifies the total number of samples and classes. The error $\left(\Gamma_f\right)$ analysis is defined as,

$$\Gamma_f = \frac{1}{2}\sum_{e=1}^{K} \| \Lambda_e^f - \Xi_e^f \| \tag{24}$$

Here, Λ_e^f is the expected classification output, and the global error (Γ) of L samples is,

$$\Gamma = \sum_{f=1}^{L} \Gamma_f \tag{25}$$

Therefore, the output of the classifier (γ) is obtained with the normal and fault panels.

Pseudo code for LILNet-5

```
Input: Snowflake image $(\psi)$
Output: Normal or fault classes
Begin
    Initialize convolutional-kernel $(\Diamond)$, $\varepsilon_1, \varepsilon_2, \varepsilon_3$, global error $(\Gamma)$
    For each data $\psi$
        Compute convolutional operation
            $\wp = \Theta\left(\sum_{M,N\in\Diamond} \Diamond_{M,N} \cdot \psi_{A+M,B+N} + \varepsilon_1\right)$
        Activate ReLu function
        Perform sub-sampling $\hbar = \vartheta_{down}\{\max(g_{p,q})\}$
        Formulate $ƛ = \eta \times \Delta + \varepsilon_2$
        Evaluate output and error
            $\Omega = \Xi(\eta \times \zeta + \varepsilon_3)$
    End For
    Return $\gamma$
End
```

3.4. Segmentation of Hotspot

The panel's thermal images are collected and preprocessed after getting γ. Features like Radiomic, SIFT-based color descriptors, color moments, cumulative distribution function, Independent component analysis, and moment invariant features are extracted from the preprocessed image (α) and given to the segmentation process. The F-RCNN is used for its effective object detection mechanism; however, the ReLu will increase the computational complexity. Therefore, the ReLu6 activation function is utilized. It has the upper limit of 6; thus, it allows more floated positions and achieves more precise output. The faster-R-CNN $\left(\Psi_{faster}\right)$ enclosed region proposal network (ϖ) and fast-RCNN $\left(\Psi_{fast}\right)$, and it is expressed as,

$$\Psi_{faster} = \varpi + \Psi_{fast} \tag{26}$$

The number of features extracted (α_{out}) from input features (α_{in}) with padding (ς) and stride (∇) along with kernel (κ) and ReLu6 activation (ι) is utilized as,

$$\alpha_{out} = \left(\frac{\alpha_{in} + 2\varsigma - \kappa}{\nabla}\right) + 1 \tag{27}$$

$$\iota = \min(\max(\alpha, 0), 6) \tag{28}$$

Thereafter, α_{out} is propagated to ϖ for region proposal $(\vee)$ generation, which is expressed as,

$$\varpi_{out} = \sum \vee(\alpha_{out}) \tag{29}$$

Here, ϖ_{out} is output from ϖ that is given to Region of Interest (ROI) pooling (Φ) along with high dimensional features (α_{out}^{*}) to transform the features into uniform size as,

$$\Phi = \varpi_{out} + \alpha_{out}^{*} \tag{30}$$

Lastly, the Φ output is passed to a fully connected layer (δ) and attains the detected damage (ξ) in a bounding box (β) as,

$$\delta_{out} = \beta(\xi) \tag{31}$$

Afterward, the segmented output (δ_{out}) undergoes an evaluation for calculating the amount of power loss (υ') for predicting the damage percentage of the fault panels, and it is computed as,

$$\upsilon' = \upsilon_{in} - \upsilon_{out} \tag{32}$$

Here, $\upsilon_{in}, \upsilon_{out}$ are the input and output power. The damage percentage (ρ) of panels is estimated with high, moderate, and low υ' as,

International Journal on Recent and Innovation Trends in Computing and Communication
ISSN: 2321-8169 Volume: 11 Issue: 9
***Article Received:** 25 July 2023 **Revised:** 12 September 2023 **Accepted:** 30 September 2023*

$$\rho = \begin{cases} 75\% < \rho \leq 100\%, & if\ High\ \upsilon' \\ 25\% < \rho \leq 75\%, & if\ Moderate\ \upsilon' \\ 1\% \leq \rho \leq 25\%, & if\ Low\ \upsilon' \end{cases} \tag{33}$$

Thus, ρ of the fault panel was effectively estimated. In the below phase, the proposed technique's performance analysis is discussed.

4. RESULT AND DISCUSSION

Here, the methodology's performance assessment is conducted using a publicly available dataset. The proposed system has been implemented on the MATLAB platform.

4.1 Dataset Description

This work utilizes a PV system thermography dataset to train the classifier with 837 images as well as 5 fault classes. The 5 fault classes are categorized as Multi-Cell Hotspot, PID defect, Single Cell Hotspot image, Diode Fault, and Dust and Shadow Hotspot. This work utilizes 80% of images for training and 20% for testing.

Table 1: Image Analysis

Hotspot/Process	Input Image	Preprocessing	Segmentation
Diagonal Crack	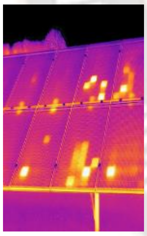	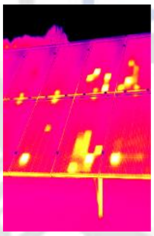	
Two Spot	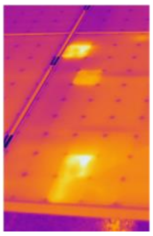	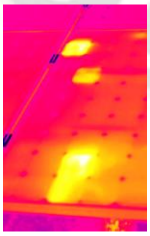	
One Spot	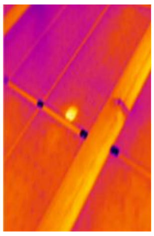	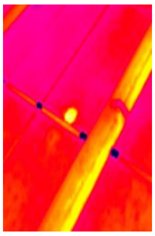	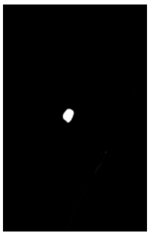
Parallel Crack	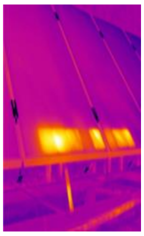		
Perpendicular Crack	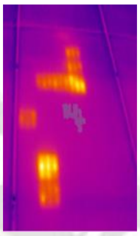		

The preprocessing and segmentation of PV panel hotspot images of diagonal, one-spot, two-spot, parallel, and perpendicular hotspots are presented in Table 1.

4.2 Performance Analysis

Here, the performance and comparative analysis of proposed models are done with existing algorithms along with related works.

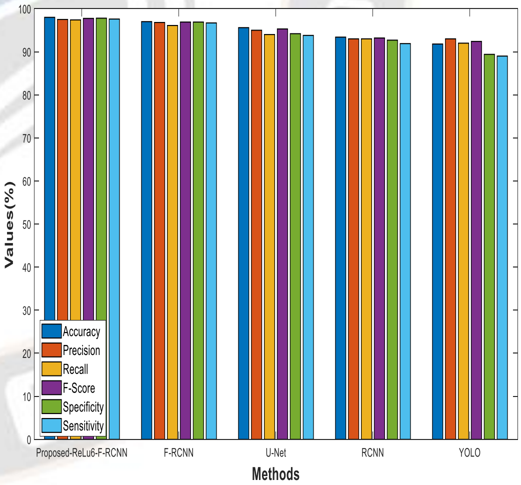

Figure 3: Performance Analysis

The proposed ReLu6-F-RCNN's performance assessment with prevailing F-RCNN, U-Net, RCNN, and YOLO is displayed in Figure 3. The ReLu6-F-RCNN approach effectively detected and segmented the hotspots with high accuracy, precision, recall, F-score, Specificity, and Sensitivity of 98%,97.5%, 97.4%, 97.75%, 97.8%, and 97.6%, correspondingly, by its quick learning ability. Nevertheless, the existing works attained comparatively low accuracy, precision, recall, F-score, Specificity, and Sensitivity. Hence, the proposed model outperformed all existing works.

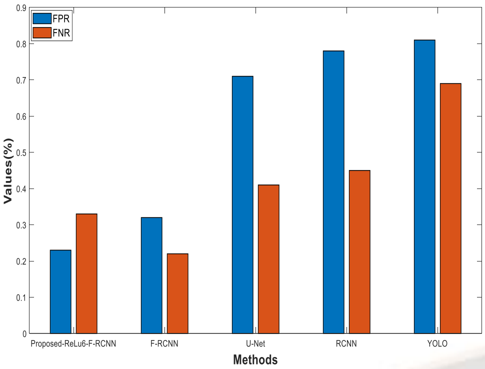

(a)

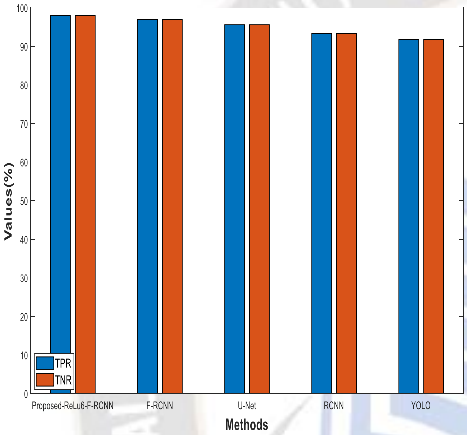

(b)

Figure 4 (a) & (b): Comparative analysis

Figures 4 (a) and (b) compare proposed ReLu6-F-RCNN with existing algorithms grounded on True Negative Rate (TNR), False Negative Rate (FNR), True Positive Rate (TPR), False Positive Rate (FPR). The ReLu6-F-RCNN model ignored the unwanted information from thermal images, so it attained 98% of TPR and TNR and has a very low FPR of 0.23 and FNR of 0.33. In contrast, the existing work has an average TPR and TNR of 94.45% but had higher average FPR of 0.65 and FNR of 0.44. These results demonstrated that the proposed ReLu6-F-RCNN model is highly efficient.

Table 2: IOU evaluation

Techniques	IOU (%)
ReLu6-F-RCNN	91.4
F-RCNN	91
U-Net	89.62
RCNN	86.07
YOLO	84.88

The Intersection Over Union (IOU) evaluation of the ReLu6-F-RCNN model with the existing algorithms is displayed in Table 2. The ReLu6 activation achieved an impressive IOU score of 91.4% for precise segmentation. In contrast, the existing algorithms attained average IOU scores of 87.89%. Therefore, the proposed model outperforms all prevailing mechanisms with its segmentation accuracy.

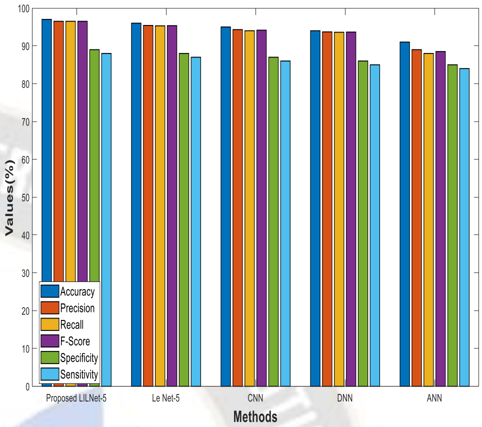

Figure 5: Performance assessment

Figure 5 displays the performance assessment of the proposed LILNet-5 and existing Deep Neural Network (DNN), LeNet5, CNN, and Artificial Neural Network (ANN). The LILNet-5 is a low-complex structure, so it effectively classified the normal and fault PV panel. Therefore, it achieved better accuracy (97%), precision (96.5%), recall (96.5%), F-score (96.5%), specificity (89%), and sensitivity (88%). Existing techniques attained comparatively low accuracy, precision, recall, F-score, specificity, and sensitivity. This result exhibited that the fault PV panels are effectively classified by the proposed model.

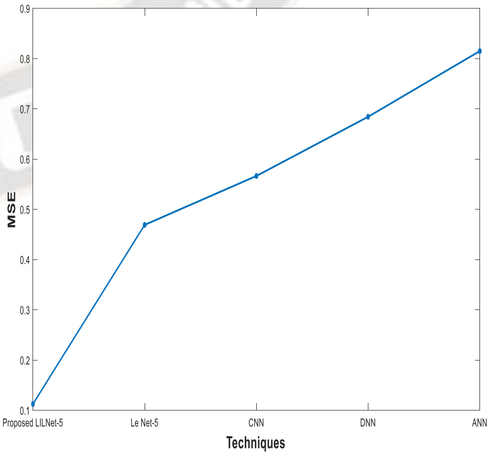

Figure 6: MSE evaluation

Table 3: Comparative Analysis of LILNet-5

Techniques	RMSE
LILNet-5	0.33541
Le Net-5	0.68491
CNN	0.7526
DNN	0.82716
ANN	0.90277

Figure 6 and Table 3 exemplify the proposed LILNet-5 and existing models' Mean Square Error (MSE) as well as Root-MSE (RMSE) evaluation. Better model performance is indicated by a lower error. The proposed LILNet-5 achieved an impressively low MSE value of 0.1125 and RMSE of 0.33541, and the existing algorithms attained the highest MSE and RMSE values. These results demonstrated that the proposed model is less error-prone with superior performance in hotspot detection.

Table 4: Comparison Analysis with related work

Study	Method	Dataset	Accuracy %	Precision %	Recall %	F-score %
Proposed	ReLu6-F-CNN	Photovoltaic system thermography	98	97.5	97.4	97.75
Fonseca Alves et al., 2021	CNN	Infrared Solar module	78.85	92	93	92
Winston et al., 2021	SVM	-	92	-	-	-
Ali et al., 2020	SVM	-	96	96.1	-	97.75
Hwang et al., 2021	CNN &XG BOOST	Thermography Inspection	95	-	-	-
Manno et al., 2021	CNN	-	97	-	-	-

Concerning precision, F-score, accuracy, and recall, the comparison analysis is shown in Table 4. For hotspot detection and classification, existing work utilizes the CNN and SVM networks. Owing to misclassification issues by detecting only fault panels, it attains only an average of 91% accuracy in hotspot detection. But, the proposed work has an efficient segmentation and classification model for PV hotspot detection and achieved higher accuracy (98%), precision (97.5%), recall (97.4%), and F-score (97.75) in hotspot detection. This significant performance improvement is the result of the modified ReLu6-F-RCNN segmentation model and LILNet-5 classification model, which accurately segmented the PV hotspots.

5. CONCLUSION

By utilizing the LILNet-5 and ReLu6-F-RCNN models, this paper introduced a thermal image-centric hotspot detection system for solar panels. In this system, PV panels, which are controlled by an MPPT controller, are equipped with DC/DC converters for output-voltage regulation. The PV panel's hotspots are effectively classified by LILNet-5, whereas ReLU6-F-RCNN segments the hotspots along with the damage percentage. The final outcomes depicted a segmentation accuracy of 98% along with a high IOU of 91.4%. The proposed model outperformed prevailing approaches and reinforced its efficiency and effectiveness in PV-panel hotspot detection.

Future Recommendations

Various types of hotspots in PV modules are successfully identified by this research. Detecting the hot-spotted panel's location may be addressed using alternative methodologies in the future.

REFERENCES

[1] Afifah, A. N. N., Indrabayu, Suyuti, A., & Syafaruddin. (2020). Hotspot detection in photovoltaic module using otsu thresholding method. *2020 IEEE International Conference on Communication, Networks and Satellite, Comnetsat 2020 - Proceedings*, 408–412. https://doi.org/10.1109/Comnetsat50391.2020.9328987

[2] Afifah, A. N. N., Indrabayu, Suyuti, A., & Syafaruddin. (2021). A new approach for hot spot solar cell detection based on multi-level otsu algorithm. *Proceedings - 2021 International Seminar on Intelligent Technology and Its Application: Intelligent Systems for the New Normal Era, ISITIA 2021*, 278–282. https://doi.org/10.1109/ISITIA52817.2021.9502239

[3] Ali, M. U., Khan, H. F., Masud, M., Kallu, K. D., & Zafar, A. (2020). A machine learning framework to identify the hotspot in photovoltaic module using infrared thermography. *Solar Energy*, *208*, 643–651. https://doi.org/10.1016/j.solener.2020.08.027

[4] Chen, J., Li, Y., & Ling, Q. (2020). Hot-Spot detection for thermographic images of solar panels. *Proceedings of the 32nd Chinese Control and Decision Conference, CCDC 2020*, 4651–4655. https://doi.org/10.1109/CCDC49329.2020.9164255

[5] Espinosa, A. R., Bressan, M., & Giraldo, L. F. (2020). Failure signature classification in solar photovoltaic plants using RGB images and convolutional neural networks. *Renewable Energy*, *162*, 249–256. https://doi.org/10.1016/j.renene.2020.07.154

[6] Fonseca Alves, R. H., Deus Junior, G. A. de, Marra, E. G., & Lemos, R. P. (2021). Automatic fault classification in photovoltaic modules using convolutional neural networks. *Renewable Energy*, *179*, 502–516. https://doi.org/10.1016/j.renene.2021.07.070

---

[7] Hong, F., Song, J., Meng, H., Rui, W., Fang, F., & Guangming, Z. (2022). A novel framework on intelligent detection for module defects of PV plant combining the visible and infrared images. *Solar Energy*, *236*, 406–416. https://doi.org/10.1016/j.solener.2022.03.018

[8] Hwang, H. P. C., Ku, C. C. Y., & Chan, J. C. C. (2021). Detection of malfunctioning photovoltaic modules based on machine learning algorithms. *IEEE Access*, *9*, 37210–37219. https://doi.org/10.1109/ACCESS.2021.3063461

[9] Kandeal, A. W., Elkadeem, M. R., Thakur, A. K., Abdelaziz, G. B., Sathyamurthy, R., Kabeel, A. E., Yang, N., & Sharshir, S. W. (2021). Infrared thermography-based condition monitoring of solar photovoltaic systems: A mini review of recent advances. *Solar Energy*, *223*, 33–43. https://doi.org/10.1016/j.solener.2021.05.032

[10] Manno, D., Cipriani, G., Ciulla, G., Dio, V. Di, Guarino, S., & Brano, V. Lo. (2021). Deep learning strategies for automatic fault diagnosis in photovoltaic systems by thermographic images. *Energy Conversion and Management*, *241*, 1–17. https://doi.org/10.1016/j.enconman.2021.114315

[11] Pathak, S. P., Patil, S., & Patel, S. (2022). Solar panel hotspot localization and fault classification using deep learning approach. *Procedia Computer Science*, *204*, 698–705. https://doi.org/10.1016/j.procs.2022.08.084

[12] Phoolwani, U. K., Sharma, T., Singh, A., & Gawre, S. K. (2020). IoT based solar panel analysis using thermal imaging. *2020 IEEE International Students' Conference on Electrical, Electronics and Computer Science*, *SCEECS 2020*, 1–5. https://doi.org/10.1109/SCEECS48394.2020.114

[13] Pramana, P. A. A., & Dalimi, R. (2020). Large scale photovoltaic (PV) farm hotspot detection using fish eye lens. *2020 IEEE Student Conference on Research and Development*, *SCOReD 2020*, 505–509. https://doi.org/10.1109/SCOReD50371.2020.9251016

[14] Rahaman, S. A., Urmee, T., & Parlevliet, D. A. (2020). PV system defects identification using remotely piloted aircraft (RPA) based infrared (IR) imaging: A review. *Solar Energy*, *206*, 579–595. https://doi.org/10.1016/j.solener.2020.06.014

[15] Su, B., Chen, H., Liu, K., & Liu, W. (2021). RCAG-Net: residual channelwise attention gate network for hot spot defect detection of photovoltaic farms. *IEEE Transactions on Instrumentation and Measurement*, *70*, 1–14. https://doi.org/10.1109/TIM.2021.3054415

[16] Venkatesh, S. N., Jeyavadhanam, B. R., Sizkouhi, A. M. M., Esmailifar, S. M., Aghaei, M., & Sugumaran, V. (2022). Automatic detection of visual faults on photovoltaic modules using deep ensemble learning network. *Energy Reports*, *8*, 14382–14395. https://doi.org/10.1016/j.egyr.2022.10.427

[17] Vergura, S. (2021). Correct settings of a joint unmanned aerial vehicle and infrared camera system for the detection of faulty photovoltaic modules. *IEEE Journal of Photovoltaics*, *11*(1), 124–130. https://doi.org/10.1109/JPHOTOV.2020.3033777

[18] Wang, X., Yang, W., Qin, B., Wei, K., Ma, Y., & Zhang, D. (2022). Intelligent monitoring of photovoltaic panels based on infrared detection. *Energy Reports*, *8*, 5005–5015. https://doi.org/10.1016/j.egyr.2022.03.173

[19] Winston, D. P., Murugan, M. S., Elavarasan, R. M., Pugazhendhi, R., Singh, O. J., Murugesan, P., Gurudhachanamoorthy, M., & Hossain, E. (2021). Solar PV's micro crack and hotspots detection technique using NN and SVM. *IEEE Access*, *9*, 127259–127269. https://doi.org/10.1109/ACCESS.2021.3111904

[20] Zefri, Y., Sebari, I., Hajji, H., & Aniba, G. (2022). Developing a deep learning-based layer-3 solution for thermal infrared large-scale photovoltaic module inspection from orthorectified big UAV imagery data. *International Journal of Applied Earth Observation and Geoinformation*, *106*, 1–13. https://doi.org/10.1016/j.jag.2021.102652